Biocybernetics and Biomedical Engineering 45 (2025) 62–73

Contents lists available at ScienceDirect

Biocybernetics and Biomedical Engineering

journal homepage: www.elsevier.com/locate/bbe

Impact of aging on anterior segment morphology and aqueous humor dynamics in human Eyes: Advanced imaging and computational techniques

Alireza Karimi [a,b,*], Marie Darche [c,d], Ansel Stanik [a], Reza Razaghi [a], Iman Mirafzal [e], Kamran Hassani [f], Mojtaba Hassani [a], Elizabeth White [a], Ivana Gantar [g], Stéphane Pagès [g], Laura Batti [g], Ted S. Acott [a,h], Michel Paques [c,d]

[a] Department of Ophthalmology, Casey Eye Institute, Oregon Health & Science University, Portland, OR, United States
[b] Department of Biomedical Engineering, Oregon Health & Science University, Portland, OR, United States
[c] Paris Eye Imaging Group, 15-20 Hôpital National de la Vision, INSERM-DHOS Clinical Investigation Center, 1423 Paris, France
[d] Sorbonne Université, INSERM, CNRS, Institut de la Vision, Paris, France
[e] Department of Mechanical Engineering, University of Nevada, Reno, Nevada, United States
[f] School of Mechanical, Industrial & Aeronautical Engineering, University of the Witwatersrand, Johannesburg, South Africa
[g] Wyss Center for Bio- and Neuroengineering, Geneva, Switzerland
[h] Department Chemical Physiology & Biochemistry, School of Medicine, Oregon Health & Science University, Portland, OR, United States

ARTICLE INFO

Keywords:
Aging
Anterior Segment
Light Sheet Fluorescence Microscopy
Aqueous Humor Dynamics
Computational Fluid Dynamics

ABSTRACT

Objective: Aging results in significant structural and functional changes in the anterior segment of the eye, influencing intraocular pressure (IOP) and overall ocular health. Although aging is a well-established risk factor for primary open-angle glaucoma, a leading cause of irreversible blindness, the specific mechanisms through which aging drives morphological changes in anterior segment tissues and affects aqueous humor dynamics remain incompletely understood.

Methods: In this study, we employed cutting-edge light sheet fluorescence microscopy (LSFM) to capture high-resolution, volumetric images of cleared human donor eyes' anterior segment tissues. This advanced imaging enabled a comprehensive morphological analysis of key parameters, including central and peripheral corneal thickness (CCT and PCT), iris thickness, anterior chamber area (ACA), and ciliary body area (CBA). By integrating these morphological parameters with computational fluid dynamics (CFD) models, we analyzed aqueous humor dynamics across $n = 6$ female human donor eyes, spanning a wide age range of 5 to 94 years (all of Caucasian descent).

Results: The CCT and PCT demonstrated thinning with age, accompanied by a reduction in ACA. In contrast, the CBA remained relatively stable across all age groups. Computational fluid dynamics analysis showed a decline in aqueous humor velocity and wall shear stress, with younger eyes exhibiting higher velocities and shear stress, compared to older eyes.

Conclusion: These findings emphasize the value of integrating LSFM and CFD approaches to provide a detailed understanding of how aging impacts the anterior segment and its fluid dynamics. This study contributes to the understanding of age-related ocular changes, highlighting the importance of considering these changes in the diagnosis and management of age-related eye diseases.

1. Introduction

Primary open-angle glaucoma (POAG) is an age-related condition [1–3], where the aging processes may contribute to the onset and progression of the disease. Aging significantly impacts the elasticity or stiffness of soft biological tissues [4–7], particularly the muscle fibers [8] of the ciliary muscle (CM). As we age, protein cross-linking and a loss of elasticity alter the relationship between the CM and trabecular meshwork (TM) in the conventional aqueous outflow pathway, given their close anatomical connection. Aging also affects the surrounding ocular structures, such as the collagen fibers in the choroid and sclera, which thicken with age [9].

* Corresponding author at: Department of Ophthalmology, Casey Eye Institute, Oregon Health & Science University, Portland, Oregon, United States.
E-mail address: karimi@ohsu.edu (A. Karimi).

https://doi.org/10.1016/j.bbe.2025.01.004
Received 7 November 2024; Received in revised form 28 December 2024; Accepted 19 January 2025
Available online 24 January 2025

In addition to affecting tissue elasticity, aging has broader effects on various other functions within the eye. For example, in studies in many Western populations, IOP in healthy individuals remains stable or slightly increases with age [10–13]. A study of aqueous humor dynamics in healthy subjects aged 20–30 and over 60 found no significant age-related increase in IOP (14.7 ± 2.6 mm Hg vs 14.3 ± 2.6 mm Hg) [14]. A study in a Japanese population reported a decrease in IOP with age, attributed to factors such as blood pressure, obesity, and other cardiac risk variables [15,16]. In contrast, large demographic studies in the United States, which included all eye conditions, observed an increase in IOP with age [17,18]. Moreover, total outflow facility also decreases with age [11,19]. Tonographic studies have consistently shown age-related declines in trabecular facility, pseudofacility, and overall facility, with about a 30% decrease from those under 40 to those over 60 years of age [11,19,20], confirmed by other studies [14,21].

Early studies in elderly individuals with posterior segment tumors suggested that uveoscleral outflow accounts for no more than 25% of total aqueous outflow, whereas research in young, healthy individuals estimated it at about 36% [22]. Fluorophotometric studies showed that uveoscleral outflow contributes 54% of total aqueous drainage in young subjects, compared to 46% in older adults [14]. Also, there is a gradual decline in aqueous humor production with age, decreasing by ~15–35% between the ages of 20 and 80, around 2.4% per decade [11,12,14,19,20,23,24]. This reduction becomes more noticeable after age 60, accelerating to 1–2% per year [11,12]. Interestingly, this reduction in aqueous humor formation with age helps to balance the increasing resistance to outflow, preventing a significant rise in IOP as people age.

Ocular rigidity also increases by about 25% in older individuals compared to younger ones [19,25]. While iris permeability to fluorescein tends to rise by around 13% per decade between ages 20 and 80, this increase is not statistically significant [24]. Although total aqueous humor flow decreases with age, the turnover rate of anterior chamber aqueous humor actually increases slightly, by about 5% per decade, possibly due to a reduction in anterior chamber depth and volume [12,26]. Furthermore, it has been shown that corneal thickness decreases with age [27,28], as with advancing age, there is a loss of elasticity and increased stiffness in the cornea, leading to thinner corneas.

To effectively study the morphological changes associated with aging and their correlation to aqueous humor dynamics, high-resolution imaging of the anterior segment tissues is crucial. Clearing is a specialized tissue processing technique that removes light-obstructing lipids, making tissues optically transparent for more precise imaging. Our recently developed advanced light sheet fluorescence microscopy (LSFM) technique has significantly enhanced this process, enabling volumetric imaging of immunolabeled, cleared samples with far quicker acquisition times compared to traditional confocal microscopy [29–32]. LSFM excels in analyzing large and complex structures, offering a more efficient and detailed alternative to the time-consuming and often artifact-prone reconstruction methods that rely on traditional histological tissue sections [33,34]. Various protocols for tissue clearing and labeling have been established, with CLARITY, BABB, 3DISCO, and CUBIC being among the most widely used [35–38]. Conducting histopathological analysis of the entire eye is particularly challenging due to its intricate composition, where neuronal, vascular, glial, pigmented, mesenchymal, and immune cells are interwoven within a collagenous shield and vitreous gel [39]. The spherical shape of the eye further complicates three-dimensional reconstructions from traditional sections, often leading to distortions. Tissue clearing provides an elegant solution to these challenges, enabling the study of intact eyes without the limitations of section-based analysis. Despite its potential, the application of tissue clearing to ocular tissues has been limited. Recent advancements have successfully utilized LSFM to image entire murine eyes, capturing the detailed organization of vascular development, particularly the hyaloid vessels [40–45]. However, the use of tissue clearing in human eyes has primarily focused on specific regions, such as the anterior segment and the sclera [46,47].

In this study, we aim to expand the application of LSFM to investigate aging-related changes in the anterior segment of human eyes. By employing this advanced imaging technique, we aim to reconstruct the morphology of the anterior segment tissues, and then calculate the morphological parameters, *i.e.*, central and peripheral corneal thickness (CCT & PCT), iris thickness (IT), anterior chamber area (ACA), and ciliary body area (CBA). Integrating these morphological findings with computational fluid dynamics (CFD) models of aqueous humor flow, we will explore how structural changes correlate with functional outcomes across different ages (5 to 94 years old). Our group has successfully applied dynamic fluid–structure interaction and CFD to model fluid flow within the human TM [48–55]. However, we have yet to conduct morphological studies that correlate these hydrodynamic parameters with the specific morphological characteristics of the anterior segment tissues. Our approach in this study offers a significant advantage over traditional histological methods, providing a more accurate and undistorted view of the complex relationships between ocular structures. By enabling the study of large, intact portions of the eye in three dimensions, LSFM allows for a more thorough investigation of how aging influences ocular function, particularly in relation to conditions like glaucoma.

2. Materials and methods

2.1. Human donor eyes

Eye samples from n=6 female donors (Caucasian descent, 5–94 years-old) were obtained through the Lion's Gift of Sight (Saint Paul, Minnesota, USA), in accordance with the regulations set forth by the U. S. Food and Drug Administration (FDA) and the Eye Bank Association of America. Demographic and clinical information of donor samples, including cause of death and ocular donation status are summarized in Table 1. The study included paired donor eyes (OD and OS) from donors aged 5, 40, 47, and 75 years, while only the OD was available for the 16- and 94-year-old donors. This resulted in a total of 12 eyes analyzed. Informed consent was obtained from the donors' families, and the next of kin did not receive any financial compensation for the donation. The eye samples were harvested within 24 h post-mortem and were confirmed to be grossly normal under a dissecting microscope. The use of these samples adhered to the ethical guidelines for human subjects and tissues as outlined in the Declaration of Helsinki. By "normal" human donor eye, we refer to eyes that showed no signs of ocular diseases, deformities, or abnormalities based on the donor's comprehensive ophthalmological records. The eyes had not undergone any prior surgeries and were free from conditions such as glaucoma, age-related macular degeneration, and corneal diseases. The lens was extracted through a corneal incision due to its tendency to reopacify over time after clearing, and the samples were fixed overnight at room temperature in 4% paraformaldehyde (15710, ThermoFisher Scientific) in PBS.

Table 1
Demographic and clinical information of donor samples, including cause of death and ocular donation status.

Sample	Age	Ethnicity	Gender	OD/OS	Cause of Death
A	5	Caucasian	Female	OD & OS	Brain hypoxia
B	16	Caucasian	Female	OD	Unknown
C	40	Caucasian	Female	OD & OS	Breast cancer
D	47	Caucasian	Female	OD & OS	Pneumonia
E	75	Caucasian	Female	OD & OS	Unknown
F	94	Caucasian	Female	OD	Sepsis due to acute kidney injury

Importation of these samples into France was conducted in compliance with the relevant regulations governing the transfer of human tissues (CODECOH DC-2015–2400). All applicable ethical guidelines related to research involving human participants were strictly followed [56].

2.2. ClearEye protocol and bleaching

The ClearEye for intact human eyes was developed in our prior publication [56] as schematically shown in Fig. 1. Samples were dehydrated in successive baths of phosphate buffered saline (PBS)/methanol (322415, Sigma Aldrich) (50%, 80%, and 100% methanol, 2 h each). Bleaching was done with 11% hydrogen peroxide (23613.297, vWR) in methanol, under white light (A025416, Manutan, 11 W) for 10 days with agitation.

To assist with pigment elimination, the bleaching solution was refreshed daily. During each renewal, a gentle flow toward the interior of the eye was created using a pipette. After the bleaching process, rehydration in PBS was carried out through a series of successive baths: 100% Methanol, followed by 80%, 50%, and finally 0% Methanol/PBS, each for 2 h. This was followed by four to six iterative PBS washes, each lasting 90 min, over the course of one day [56].

2.3. Labeling and clearing

To improve antibody penetration, we adapted an immunolabeling protocol from the SWITCH method [57], which enhances antibody diffusion by modulating the antibody-antigen interaction using sodium dodecyl sulfate (SDS). Samples were first permeabilized and equilibrated for four days in PBSGT-Sw solution (PBS with 0.2% gelatin, 5% Triton X-100, and 10 mM SDS) at 37°C with gentle agitation. Primary antibodies, including goat anti-Collagen IV, mouse anti-alpha-smooth muscle actin (SMA), and rabbit anti-Tubulin III, were pre-incubated separately in PBSGT-Sw for 2 h, then applied to the samples for 20 days under similar conditions. After incubation, samples were rinsed and incubated in PBSGT without SDS for 4 days to facilitate antibody binding. Secondary antibodies, filtered and diluted in PBSGT, were then incubated with the samples in darkness for 48 h at 37°C. Post-incubation, samples were washed and re-fixed in 4% paraformaldehyde for 45 min to prevent tissue softening during clearing.

For the clearing process, samples were dehydrated through a series of PBS/methanol baths, starting with 20% methanol overnight, followed by sequential baths of 40%, 60%, 80%, and twice in 100% methanol for 2 h each. The samples were then soaked overnight in a solution of two-thirds dichloromethane (DCM) and one-third methanol. Afterward, they were immersed in 100% DCM for 45 min, followed by dibenzyl Ether (DBE). The DBE baths were refreshed every 2 h until the solution appeared clear with no visible swirls upon gentle agitation. Finally, the cleared samples were stored in DBE in the dark, where they remained stable and retained transparency and immunofluorescence for at least one year [56].

2.4. Imaging

For imaging, the cleared human eyes were placed in an immersion quartz cuvette (3 cm × 3 cm × 4 cm) filled with DBE as the imaging medium [45,56]. Imaging was conducted using a custom-made meso-scale selective plane-illumination microscope (mesoSPIM) at the Wyss Center in Geneva, enabling full-eye imaging with a travel range of 44 × 44 × 100 mm, producing near-isotropic resolution 3D datasets [58]. The sample was illuminated by one of two digitally scanned light sheets from opposite directions, with galvo scanners integrated into the excitation paths to generate the light sheet and minimize shadow artifacts. The beam waist was scanned using electrically tunable lenses synchronized with the sCMOS camera's rolling shutter, resulting in uniform axial resolution across the field of view (FOV).

Fluorescence emissions were captured using an Olympus MVX-10 zoom microscope with a 1× objective (Olympus MVPLAPO 1×) and recorded on a Hamamatsu ORCA-Flash 4.0 digital camera at 5 frames per second. The excitation wavelengths for autofluorescence, and 561 and 647 nm labels were set at 488, 561, and 647 nm, respectively, with

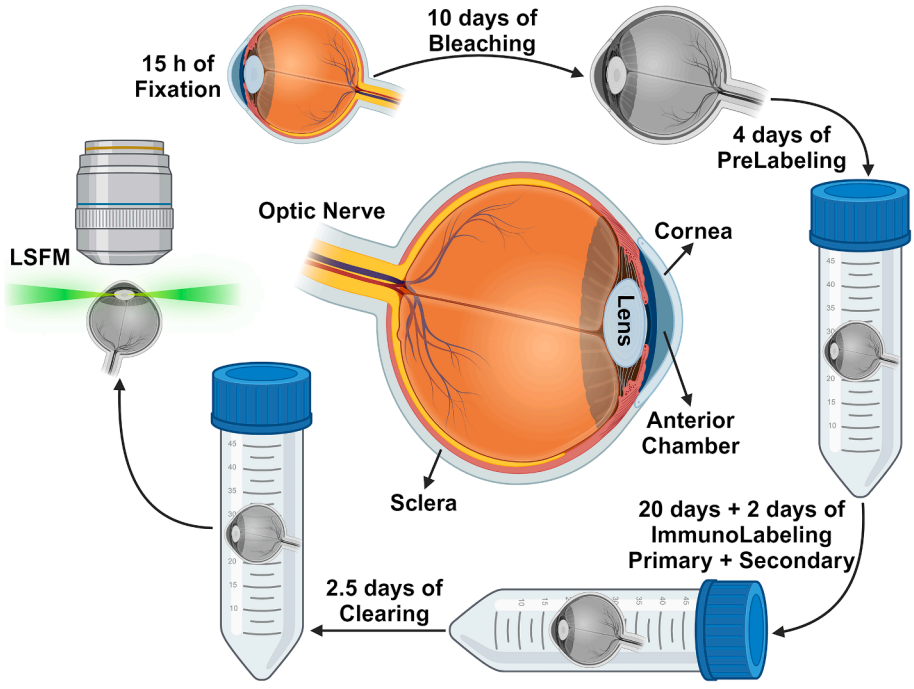

Fig. 1. Schematic representation of the ClearEye protocol for preparing whole human eyes for light sheet fluorescence microscopy (LSFM). The process begins with 15 h of fixation, followed by 10 days of bleaching to remove pigmentation. After bleaching, the sample undergoes 4 days of pre-labeling with primary antibodies. This is followed by 20 days of primary immunolabeling and an additional 2 days for secondary antibody labeling. The eye is then cleared over 2.5 days to achieve optical transparency. Finally, the prepared eye is imaged using LSFM, enabling detailed 3D visualization of the ocular structures. This figure is adapted from the concept of Fig. 1a in our recent publication [56], with rights and permissions already obtained.

emission filters of 530/40 nm bandpass, 593/40 bandpass, and 663 LP (BrightLine HC, AHF). All acquisitions were performed from a single orientation of the eye using a multi-tile setup (2 × 2) with dual-side illumination to enhance image quality and light penetration. To accommodate the large sample size, z-sub-stacks were acquired at different focal ranges with a zoom setting of 0.8X at 5 μm spacing, resulting in an in-plane pixel size of 8.2 × 8.2 μm (2048 × 2048 pixels). This resulted in an undersampled 3D image based on the Nyquist sampling rule, with the effective detection numerical aperture (NA) of the MVX-10/MVPLAPO estimated at 0.065 at 0.8X, yielding a diffraction-limited lateral resolution of 3.8 μm. The data acquisition for a single eye took less than half a day, including the setup, multi-tile imaging, and z-stack acquisition. This timeframe ensured high-resolution and comprehensive datasets while maintaining tissue integrity.

2.5. Data analysis

Following data acquisition, the z-sub-stacks were concatenated using Image J, and the tiles were assembled into 3D models with the Grid Collection Stitching plugin in TeraStitcher (BMC Bioinformatics, Italy). The resulting HdF5 files were converted to *.ims* format for further analysis using ImarisBitplane software or the virtual reality platform Syglass. Imaris software (versions 10.1, Bitplane) was utilized to render and examine the samples in 3D as displayed in Fig. 2. To isolate specific ocular structures and vascular beds, built-in tools for slicing, manual segmentation, and 3D rendering were employed. Imaris also provided animation and snapshot tools for capturing video and images. Fig. 3 illustrates the cross-sectional images of the anterior segment from human donor eyes across various age groups. To quantitatively compare the morphological characteristics between these groups, we defined several key parameters, including central corneal thickness (CCT), peripheral corneal thickness (PCT), anterior chamber area (ACA), iris thickness (IT), and ciliary body area (CBA), as displayed in Fig. 4. These parameters were measured at the corneal apex in the cross-sectional images of the donor eyes, providing a detailed assessment of age-related changes in anterior segment morphology. The ACA was measured after the lens was removed using the remaining anatomical landmarks to ensure consistent and reproducible measurements. Specifically, the boundaries for ACA were defined as the area enclosed by the posterior corneal surface, the anterior surface of the iris, and the plane of the iridocorneal angle. This approach allowed us to maintain uniformity in ACA measurements across all samples. Regarding the measurement of the CBA. After lens removal, CBA was defined and measured using consistent anatomical boundaries, specifically the posterior surface of the iris and the inner scleral wall, extending to the outermost boundary of the ciliary body. These landmarks were selected to ensure accurate and reproducible measurements across all samples. To ensure the reliability of our measurements, we assessed reproducibility by performing repeated analyses on a single sample per age group. These analyses were conducted using a Python-based program to standardize measurements and minimize user bias. The results demonstrated high consistency, confirming the robustness of our methodology.

2.6. Segmentation and 3D Finite Element mesh reconstruction

A custom Python program was developed to segment the flow region within the anterior chamber, extending from the ciliary body to the SC lumen based on the cross-sectional images of the human donor eyes at different age groups (Fig. 3). Given that the TM lies between the anterior chamber and the SC lumen, it was excluded from the segmentation to establish a direct connection for the flow between the anterior chamber and the very simplified SC lumen structure. The segmented flow regions were then volume-meshed with a uniform thickness of 40 μm [59–61]. This resulting volume mesh accurately represented the flow regions within our eye models at an aqueous humor pressure of 0 mm Hg. The lens geometry was added to the model based on the data in the literature [62]. We want to acknowledge that the geometry of the TM region used in this study is highly simplified. Specifically, we connected the elements in the iridocorneal angle to the SC lumen through a porous representation of the TM/JCT/SC complex. This approach was chosen deliberately, as the primary focus of this study is to explore the effects of aging on anterior segment morphology and its general impact on aqueous humor dynamics, rather than providing a detailed analysis of the hydrodynamics within the outflow pathway. A more refined representation of this region would be necessary for future studies focusing specifically on outflow resistance and related mechanisms.

2.7. Computational fluid dynamics (CFD)

Our CFD models employed 8-noded hexahedral elements. A constant IOP of 15 mm Hg was applied to all models across different ages, with an outlet pressure of 9 mm Hg at the episcleral venous. This approach was intentionally chosen to isolate the effects of age-related geometric changes on aqueous humor dynamics. By maintaining consistent inlet and outlet pressures across models, we aimed to ensure that the results primarily reflect morphological differences due to aging, rather than

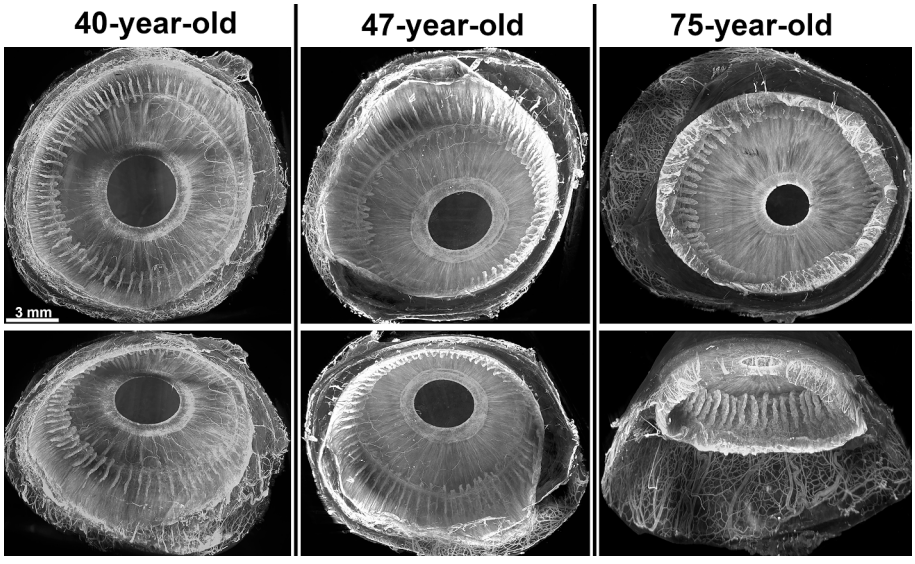

Fig. 2. 3D segmented images of the anterior segment tissues from donor eyes aged 40, 47, and 75 years, generated using Imaris software.

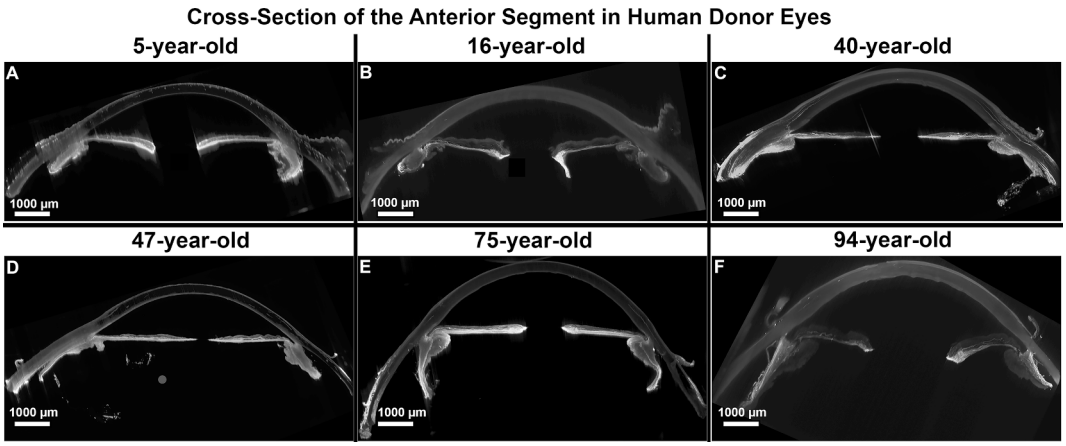

Fig. 3. Cross-sectional images of the anterior segment in human donor eyes across different ages, ranging from 5 years to 94 years old. The images reveal age-related morphological changes, including variations in corneal thickness, anterior chamber area, iris thickness, and ciliary body morphology. These alterations may reflect the natural aging process of ocular tissues and their implications for conditions such as glaucoma. Scale bar: 1000 µm.

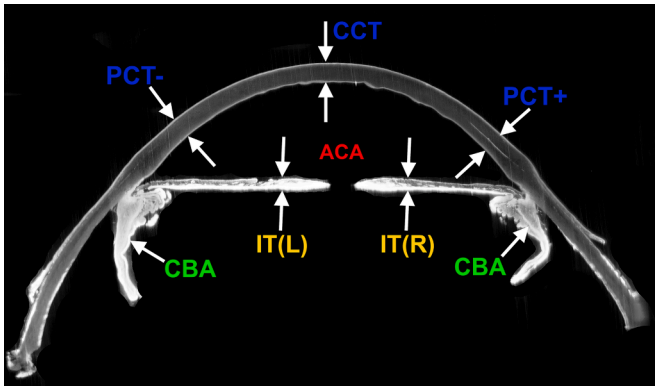

Fig. 4. Cross-sectional representation of the morphological parameters of the anterior segment. PCT-: Peripheral corneal thickness (left); PCT+: Peripheral corneal thickness (right); CCT: Central corneal thickness; ACA: Anterior chamber area; IT(L): Iris thickness (left); IT(R): Iris thickness (right); CBA: Ciliary body area.

being influenced by variations in boundary conditions.

The permeability was also added to the fluid across the TM/JCT/SC complex. Thus, our model incorporated both porous and non-porous domains with appropriately defined interfaces to ensure accurate interaction between the regions. The permeability characterizes the ability of a porous material to diffuse fluids. This parameter is used to define the resistance of the outflow through the TM. Darcy's law defines permeability [63]:

$$\alpha = \frac{\mu}{\Delta P}\Delta eV \tag{1}$$

where α is the permeability, ΔP is the pressure change, μ is the viscosity, Δe is the thickness of the porous domain, and V is the velocity component. The dynamic viscosity (µ) is considered 0.7185×10^{-3} Pa·s, the thickness of the tissue in the flow direction (Δe) is ~30–80 µm, the pressure drop is assumed to be ~ 6 mm Hg, and the velocity component reflects a 0.008 mm/s (decided after several trial and errors based on [64]) of value in the modeling to calculate the porosity coefficient (α). The viscous resistance (inverse absolute permeability) is given to Ansys Fluent software with a specific flow direction in the performed simulation to determine flow behavior in a porous model of the tissue and a proper pressure drop along the porous material. The TM/JCT/SC complex resistance to outflow determines the pressure drop between the anterior chamber and the episcleral veins. Several permeability values were tested to drop the IOP through the domain. In this model, the permeability coefficient (α) was set to 2×10^{-15} m^2.

Our CFD simulation was conducted on a workstation equipped with a 112-core Intel® Xeon® Gold 6258R CPU clocked at 2.70 GHz and 1 TB of RAM, using Ansys/Fluent. The loading was applied incrementally over a 0.5-second period. On average, the simulations took ~30 min to complete on this workstation [49–52,54,55].

2.8. Statistical analyses

Data was collected on the following metrics: CCT, PCT (+20, −20, +40, and −40), IT (L and R), CBA, ACA, velocity, and wall shear stress. Mixed-effects models were used to find the mean and standard error for each metric. Mixed-effects models were used to see if any of the metrics were associated with the patient's age. Mixed-effects models were used to see if any of the metrics were associated with one another. x10 for Bonferroni corrections were used when comparing metric to one another, but x11 Bonferroni correction was used for comparing age to each metric. Mixed-effects models were created using the *lmer* function from the *lmerTest* package (version 3.1–3) in R version 4.4.1.

3. Results and Discussions

The analysis of the CCT shows a clear trend of thinning with increasing age. As observed in Table 2, the slope of −0.323 ($p > 0.99$) suggests a decrease in CCT with advancing age, although the change is

Table 2
Summary of associations between metrics and patient's age.

Variable	Slope (SE)[1,2]	Marginal R-Squared[1]	Conditional R-Squared[1]	*P*-Value[1]
CCT	−0.3232 (0.2364)	0.1719	0.1719	> 0.99
PCT + 20	−0.2792 (0.2137)	0.1688	0.2705	> 0.99
PCT −20	0.07266 (0.1841)	0.0216	0.5655	> 0.99
PCT + 40	−0.2631 (0.2087)	0.1507	0.1579	> 0.99
PCT −40	−0.1868 (0.1905)	0.1163	0.5117	> 0.99
IT (L)	−0.4575 (0.1393)	0.5453	0.5453	0.122
IT (R)	−0.03931 (0.2482)	0.0032	0.2954	> 0.99
CBA	25.35 (207.1)	0.0017	0.0017	> 0.99
ACA	−1274 (1752)	0.0555	0.0555	> 0.99
Velocity (mm/s)	−7.68e-04 (0.0002071)	0.665	0.8675	0.174
Shear (Pa)	−4.75e-07 (0.0000001426)	0.6542	0.9999	> 0.99

The measurements are based on Pixel.
[1] Values obtained from mixed-effects models.
[2] Values represent the change in each variable with a one-year increase in age.

not statistically significant in this case. The linear regression in Fig. 5 further supports this inverse relationship, showing a downward trend of CCT as age increases. This age-related thinning of the central cornea is consistent with previous studies and is significant for understanding age-related biomechanical changes in the corneal structure, which might affect IOP regulation and overall corneal health. The PCT was analyzed at different peripheral positions: +20, −20, +40, and −40 degrees. Table 2 provides the slopes indicating the changes in PCT at these positions with age. For example, PCT +20 and PCT +40 both show negative slopes (−0.2792 and −0.2631 respectively), suggesting a decrease in thickness with age, although these changes are not statistically significant ($p > 0.05$). However, PCT −20 shows a positive slope of 0.072, indicating a slight increase with age, but again, this result is not significant ($p > 0.05$). The marginal R-squared values in Table 2 suggest that changes in PCT at different angles are not well explained by age alone. For instance, PCT +20 has a marginal R-squared of 0.1688, indicating that age only accounts for about 16.88% of the variability in PCT +20, and even less in PCT −20. This suggests that factors other than age may contribute to changes in peripheral corneal thickness. Interestingly, Table 3 highlights a positive association between CCT and PCT +20, PCT+40, PCT-40, and ACA, indicating that thicker central corneas tend to have thicker peripheral corneal regions, particularly in the superior aspect of the cornea. These findings suggest that while age is an influencing factor, the central and peripheral corneal thicknesses are interrelated, indicating a more complex biomechanical relationship within the corneal structure. Our findings revealed that both CCT and PCT tend to decrease with age, but their changes are not uniformly distributed across different peripheral positions. The significant correlations between CCT and PCT imply that changes in central corneal structure may influence the peripheral corneal regions. Understanding these relationships can be crucial for clinical assessments, as alterations in corneal thickness with age may affect ocular biomechanics and visual outcomes. Our results emphasize the importance of considering both CCT and PCT when evaluating corneal health, especially in age-related conditions such as glaucoma.

The angle between the cornea and iris (iridocorneal angle) demonstrates a clear age-dependent decline, with measurements of 44.06°, 41.19°, 37.77°, 38.71°, 30.51°, and 28.82° for eyes aged 5, 16, 40, 47, 75, and 94 years, respectively. This represents a total reduction of 15.24° (34.6%) over the age range. The decline is most noticeable during mid-life and early older adulthood, with a reduction of 7.26° (19.2%) between ages 40 and 75 years. In contrast, early life (5–40 years) and late adulthood (75–94 years) show smaller declines of 6.29° (14.3%) and 1.69° (5.5%), respectively. The reduction in iridocorneal angle observed in our study aligns with *in vivo* findings that show age-related narrowing due to structural changes in the anterior segment, such as lens thickening and anterior displacement of the lens-iris diaphragm [65,66]. These changes may contribute to increasing the resistance to aqueous humor outflow and the risk of angle-closure glaucoma, especially in older populations.

The analysis of velocity and shear stress across different age groups reveals important understandings of corneal biomechanics as age progresses. Fig. 6 shows streamlines of aqueous humor velocity and wall shear stress contours. It illustrates a gradual reduction in their magnitudes in older donor eyes compared to younger ones. This decline is more apparent when comparing the velocity and shear stress values in the 5-year-old eye versus the 94-year-old eye, suggesting age-related changes in the corneal environment. This showed as a linear regression graph in Fig. 7, where a slight downward trend with advancing age is observed. This trend suggests that as the eye ages, both velocity and shear stress tend to decrease, indicating potential changes in the fluid dynamics of the aqueous humor within the anterior chamber. From Table 2, there was an insignificant negative association between patient age with velocity and shear stress. Specifically, velocity within the anterior chamber, especially the outflow region, decreases significantly, with younger eyes (*e.g.,* the 5-year-old eye) exhibiting higher velocities (~0.18 mm/s) compared to older eyes (*e.g.,* the 94-year-old eye) with velocities below ~0.09 mm/s. Similarly, wall shear stress declines moderately, decreasing from ~0.0001 Pa in younger eyes to ~0.00005 Pa in older eyes. These findings suggest that aging significantly impacts

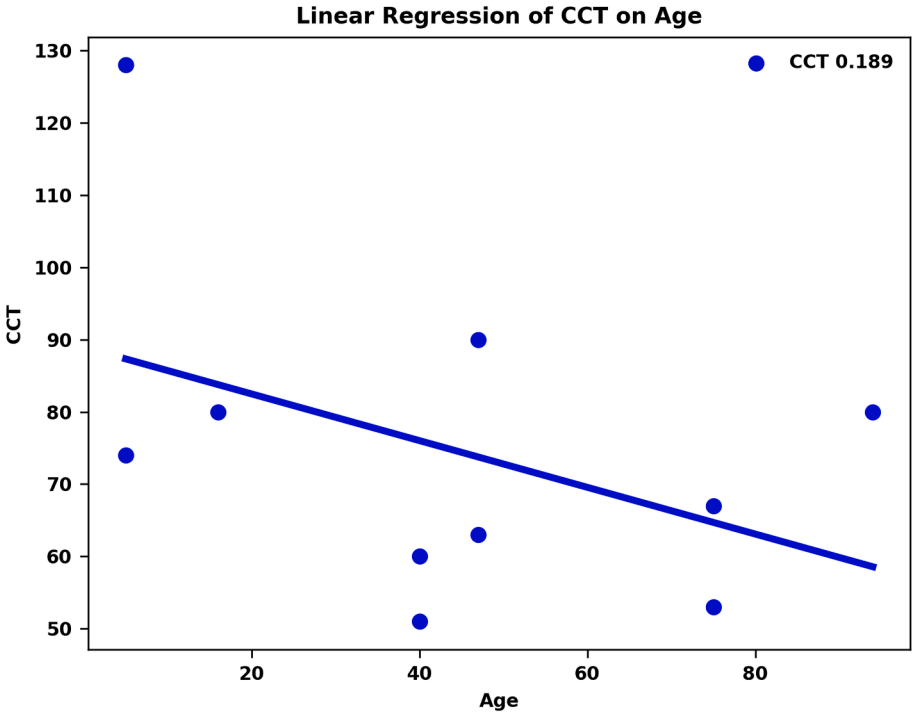

Fig. 5. Linear regression analysis showing the relationship between central corneal thickness (CCT) and age. The regression line indicates a decline in CCT with increasing age, suggesting a potential age-related thinning of the cornea. The R^2 value of 0.189 suggests a moderate association between age and CCT, highlighting individual variability within the data set.

Table 3
Summary of associations between metrics from mixed-effects models. The measurements are based on Pixel.

Variables	Slope (P-Value) CCT	PCT + 20	PCT −20	PCT + 40	PCT −40	IT (L)	IT (R)	CBA	ACA	Velocity	Shear
CCT	–	1.124 (< 0.001)	1.106 (0.475)	1.131 (< 0.001)	1.21 (0.023)	0.7745 (0.511)	−0.3815 (> 0.99)	0.0007471 (0.676)	0.0001151 (0.027)	219.1 (> 0.99)	−38390 (> 0.99)
PCT + 20	0.8588 (< 0.001)	–	0.8577 (0.848)	0.9682 (< 0.001)	1.02 (0.043)	0.6575 (0.58)	−0.5976 (0.898)	0.0006538 (0.58)	0.00009549 (0.019)	227.7 (> 0.99)	−4781 (> 0.99)
PCT −20	0.3563 (0.515)	0.3764 (0.856)	–	0.4647 (0.212)	0.6506 (0.131)	−0.0531 (> 0.99)	0.3359 (> 0.99)	0.00006707 (> 0.99)	0.00002397 (> 0.99)	−159.7 (> 0.99)	−491200 (0.629)
PCT + 40	0.853 (< 0.001)	0.9707 (< 0.001)	1.092 (0.186)	–	1.087 (0.01)	0.5721 (> 0.99)	−0.2563 (> 0.99)	0.0005334 (> 0.99)	0.00009414 (0.071)	145.6 (> 0.99)	−117500 (> 0.99)
PCT −40	0.5855 (0.023)	0.6462 (0.043)	0.856 (0.131)	0.6973 (0.01)	–	0.3368 (> 0.99)	0.1484 (> 0.99)	0.0001335 (> 0.99)	0.00004426 (> 0.99)	83.94 (> 0.99)	−123100 (> 0.99)
IT (L)	0.5118 (0.511)	0.5881 (0.498)	−0.08561 (> 0.99)	0.501 (> 0.99)	0.5713 (> 0.99)	–	−0.3695 (> 0.99)	0.0004839 (> 0.99)	0.00006166 (> 0.99)	340.3 (> 0.99)	514,500 (> 0.99)
IT (R)	−0.3361 (> 0.99)	−0.6143 (0.902)	0.715 (> 0.99)	−0.2847 (> 0.99)	0.3697 (> 0.99)	−0.3151 (> 0.99)	–	−0.0006275 (0.659)	−0.00008223 (0.245)	30.79 (> 0.99)	−473300 (> 0.99)
CBA	478.2 (0.634)	569 (0.509)	205.2 (> 0.99)	457.1 (> 0.99)	309 (> 0.99)	376.9 (> 0.99)	−516.7 (> 0.99)	–	0.08959 (0.075)	−1172 (> 0.99)	−107900000 (> 0.99)
ACA	6788 (< 0.001)	8595 (< 0.001)	3037 (> 0.99)	6705 (0.014)	5339 (0.702)	4534 (0.732)	−6081 (0.137)	6.823 (0.004)	–	1,241,000 (> 0.99)	1,499,000,000 (> 0.99)
Velocity (mm/s)	−0.0003819 (0.678)	−0.0004926 (0.476)	−0.00042 (> 0.99)	−0.000383 (> 0.99)	−0.000171 (> 0.99)	−0.0005244 (0.81)	0.0005302 (0.229)	−0.0000004482 (0.437)	−0.00000005466 (0.054)	–	1163 (0.422)
Shear (Pa)	−0.000000000 0000000005662 (> 0.99)	−0.000000000 000000001502 (> 0.99)	0.000000000000 0000003967 (> 0.99)	−0.000000000 0000008816 (> 0.99)	0.000000000 0000000006822 (> 0.99)	−0.000000000000 0000004391 (> 0.99)	−0.000000000000 00000007575 (> 0.99)	−0.000000000000 00000004621 (> 0.99)	−0.000000000000000 0000002904 (> 0.99)	0.000000000000 0002285 (> 0.99)	–

the fluid dynamics of the anterior segment, may contributing to increased outflow resistance and dysregulated IOP. This aligns with earlier studies highlighting the role of age-related changes in the outflow pathway morphology in influencing outflow resistance and IOP regulation [49–52,54,55]. The volumetric average shear stresses and velocity were used for comparison purposes.

The relationship between ACA and age, as observed in Table 3, shows a negative slope of −1274 pixels per year, although this change was not statistically significant ($p > 0.99$). This suggests that the ACA may reduce slightly with increasing age, but the variability is high, indicating considerable individual differences. Given that the ACA may influences aqueous humor dynamics and IOP regulation, this age-related trend might play a role in the biomechanical properties of the anterior segment but warrants further investigation with a larger sample size. In Table 3, ACA is shown to have correlations with both CCT and PCT measurements, indicating that changes in the peripheral or central corneal thickness correspond with variations in ACA. Our findings, while insignificant, align with previous research indicating that older eyes tend to have smaller anterior chamber volumes (160 ± 39 vs 247 ± 39 μl; $p < 0.00001$), reduced aqueous humor flow (2.4 ± 0.6 vs 2.8 ± 0.8 μl/min; $p = 0.002$), and lower uveoscleral outflow (1.10 ± 0.81 vs 1.52 ± 0.81 μl/min; $p = 0.009$) compared to younger eyes [14].

For the CBA, Table 3 presents a very minimal positive slope of 25 per year with age ($p > 0.99$), indicating almost no significant change in CBA across different age groups. This suggests that, unlike other morphological parameters, CBA remains relatively stable over time. This stability might imply that the ciliary body's role in aqueous humor production and outflow is not as influenced by age-related changes compared to other anterior segment structures in our data. The correlations between CBA and corneal parameters in Table 3 were also non-significant, suggesting that CBA's role and its potential influence on IOP and biomechanics may be relatively independent of corneal morphological changes. ACA seems to exhibit a more evident, albeit non-significant, trend with age compared to CBA, which remains largely unchanged. This suggests that the anterior chamber's ability to regulate aqueous humor dynamics might be more susceptible to age-related shifts than the ciliary body, potentially impacting IOP regulation and glaucoma risk. Specifically, prior studies have demonstrated that both nasal and temporal ciliary muscle thickness tend to increase with age ($p = 0.004$ and $p < 0.001$, respectively), which is consistent with the idea that certain aspects of ciliary muscle morphology remain robust as individuals age. Also, nasal and temporal distance from the scleral spur to the thickest point of the ciliary muscle were found to decrease with age [65], highlighting that while some elements of the ciliary body exhibit changes, the overall area (CBA) in our study did not significantly vary with age. Considering the wide age of the range of our subject as well as the lack of enough donor eyes, our conclusion may not be fully robust, needing for future investigations.

At the end we provided a correlation matrix heatmap in Fig. 8, which better represents the correlation between the parameters. The correlations indicate that aging impacts various anterior segment parameters, particularly with thinning of the cornea and iris. The strong associations between CCT and PCT highlight the need to consider corneal thickness measurements in a holistic manner rather than in isolation. Also, the relationships between CBA and ACA, as well as the strong coupling between velocity and shear stress, underscore the interconnectedness of anterior segment structures and the influence of dynamic fluid properties. These findings have potential implications for age-related ocular conditions, such as glaucoma and corneal diseases, where structural changes in the anterior segment and altered fluid dynamics play a critical role. Understanding these correlations could inform clinical assessments and treatment strategies in age-related ocular pathologies.

Data was collected from a relatively small sample of 10 eyes from n=6 patients, with ages ranging from 5 to 94 years and a mean age of 44.4 years. Given this limited sample size, it is crucial to interpret the correlations and findings with caution, as they may not be fully

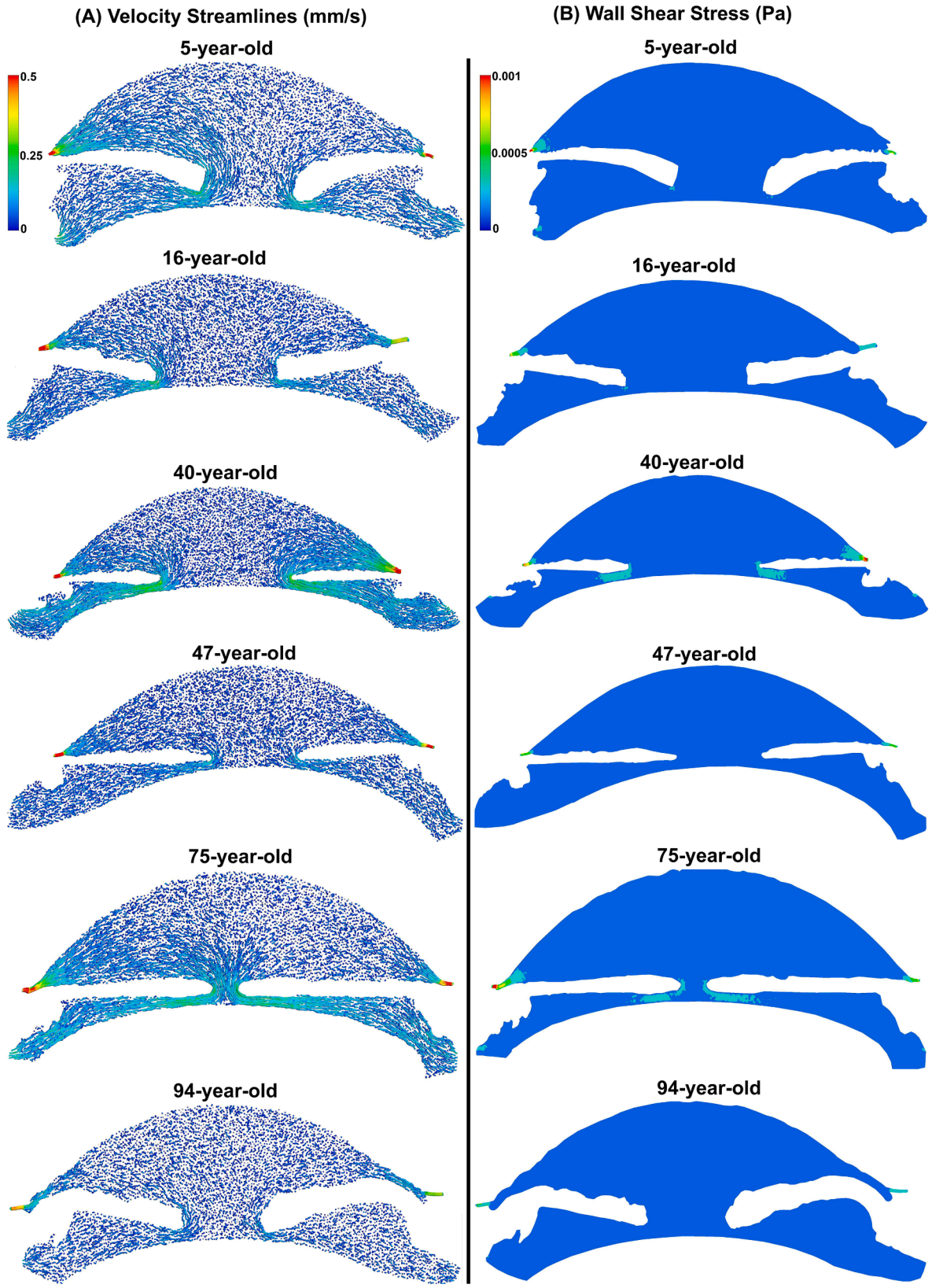

Fig. 6. **(A)** Velocity streamlines (mm/s) in the anterior segment of human donor eyes across different ages (5, 16, 40, 47, 75, and 94 years old), demonstrating the distribution of aqueous humor flow. **(B)** Wall shear stress (Pa) in the anterior segment for the same age groups, illustrating how shear stress varies with age in the human eye. The color bars indicate the magnitude of velocity and shear stress, with warmer colors representing higher values.

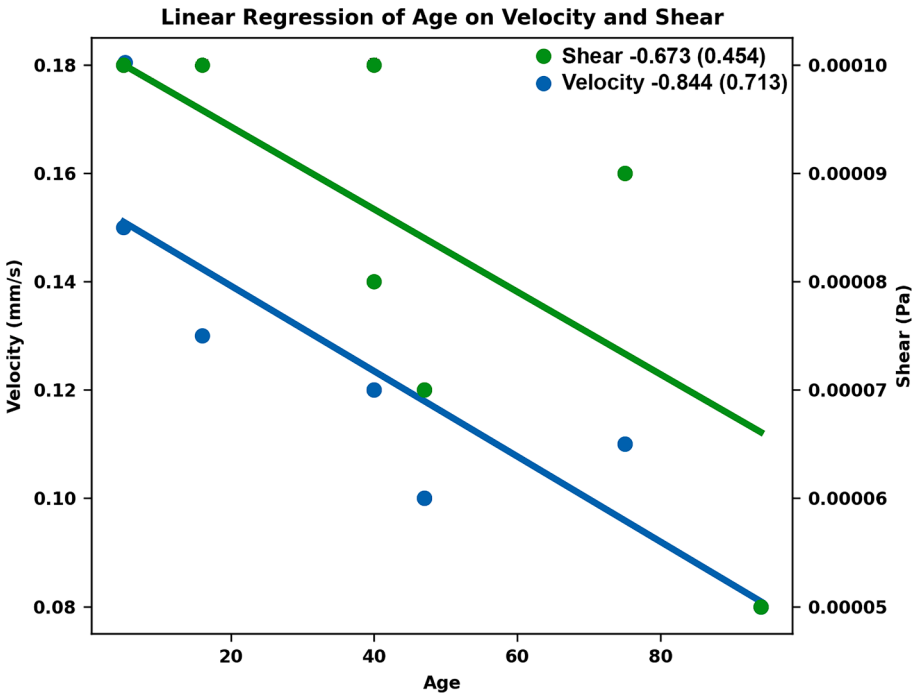

Fig. 7. Linear regression analysis of age on velocity (mm/s) and shear stress (Pa) in the anterior segment. The blue line represents the relationship between age and velocity, while the green line represents the relationship between age and shear stress. The corresponding R-squared values indicate the degree of association for each parameter.

representative of a larger or more diverse population. A larger cohort could potentially alter the strength or direction of these correlations. While we fully recognize the importance of gender as a biological variable, this study did not specifically evaluate sex differences, which could have a considerable influence on the ocular parameters observed. To ensure a more accurate and comprehensive understanding of how these factors impact ocular anatomy and physiology, future research should include a larger, more diverse sample size that accounts for sex-related variations. This approach will help clarify the potential influence of sex differences on these parameters, ultimately enhancing the robustness and applicability of the findings.

Compared to other high-resolution imaging modalities like OCT, LSFM offers unique advantages for *ex vivo* studies. LSFM enables volumetric imaging with optical sectioning, providing detailed 3D visualization of complex structures such as the TM and ciliary body. Also, it allows for a wide field of view and enhanced contrast when combined with fluorescent labeling, enabling more precise analysis of cellular and extracellular matrix features. These capabilities make LSFM particularly well-suited for investigating age-related changes in ocular morphology.

A population-based study using swept-source OCT [65] demonstrated significant reductions in anterior chamber depth and corneal thickness, as well as thinning of the iris with advancing age. These findings align with our observations of structural changes in the anterior segment and provide further evidence of age-related remodeling of ocular tissues. The consistency between *in vivo* and *ex vivo* results highlights the robustness of our methodology and underscores the importance of continued investigation into the biomechanical implications of these changes in the context of glaucoma and other age-related eye diseases.

This study uniquely integrates high-resolution LSFM with CFD modeling to investigate age-related changes in the anterior segment of the eye. By combining detailed morphological analysis with biomechanical simulations, we provided new understandings of structural changes and their implications for aqueous humor dynamics. This comprehensive approach represents a significant advancement in understanding the biomechanical effects of aging on ocular structures.

3.1. Limitations

Despite the significant findings of this study, several limitations should be acknowledged to provide a balanced understanding of the results and to guide future research.

We had limited sample size and donor variability. Our study's conclusions were based on a relatively small number of human donor eyes, which may limit the generalizability of our findings. Also, the variability among donors, including differences in age, health status, and post-mortem intervals, could introduce variations in the data that may not fully represent the broader population. To address this limitation, future studies should include a larger and more diverse sample set, with stratification based on donor characteristics such as age and health status to better account for potential sources of variability.

The LSFM has its own inherent limitations. While LSFM provides high-resolution imaging, it has limitations in capturing fine details within highly complex structures or deep tissue regions, potentially leading to incomplete morphological data. Also, the optical clearing methods employed may not fully eliminate scattering and absorption, which could result in artifacts or incomplete imaging in certain regions of the eye. To overcome these issues, complementary imaging techniques, such as confocal or multiphoton microscopy can be employed in future to validate and cross-check LSFM results. Furthermore, optimizing the clearing protocols for specific tissue types could enhance imaging quality and reduce artifacts.

Tissue degradation post-mortem and potential artifacts introduced during fixation and processing may affect the structural integrity of the samples, leading to possible distortions in the morphological analysis. Also, the removal of the lens to prevent reopacification may alter the natural anatomy, potentially impacting the study of anterior chamber dynamics. To minimize these issues, future studies should use the freshest possible samples and standardize fixation and processing protocols across all specimens. Exploring alternative fixation methods that better preserve tissue integrity or utilizing imaging techniques that allow in situ analysis could further mitigate these challenges.

Our simulations of aqueous humor flow were conducted without

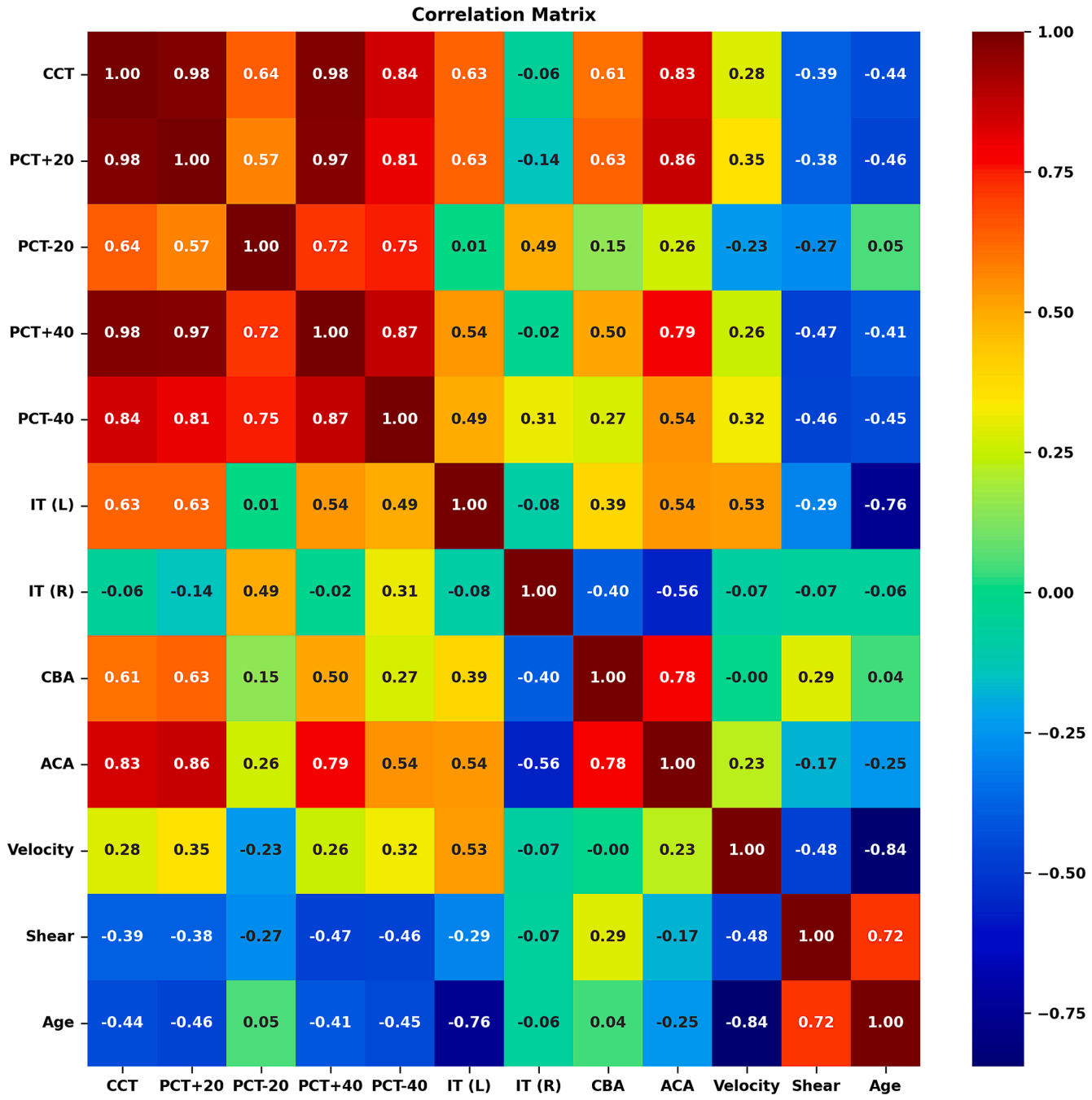

Fig. 8. Correlation matrix illustrating the relationships between various anterior segment parameters, including central corneal thickness (CCT), peripheral corneal thickness at different angles (PCT + 20, PCT −20, PCT + 40, PCT −40), iris thickness (IT), ciliary body area (CBA), anterior chamber area (ACA), velocity, shear, and age. Color intensity and gradient indicate the strength and direction of the correlations, with red representing strong positive correlations and blue indicating strong negative correlations.

direct access to lens morphology. To account for this limitation, we utilized established anatomical parameters and literature-based boundary conditions to approximate the natural flow dynamics. Lens removal might also alter ACA measurements. While this approach provides valuable understandings of the anterior segment and conventional outflow pathway, future studies incorporating lens morphology could enhance the accuracy of flow simulations.

The morphological analyses and CFD simulations were all conducted based on fixed *ex vivo* human donor eyes, which may not fully replicate the *in vivo* environment. The absence of real-time physiological conditions could limit the applicability of these findings to clinical practice. Future research should aim to validate these findings with *in vivo* data, potentially through non-invasive imaging techniques, *i.e.*, OCT, or animal models that allow for real-time observation of fluid dynamics and tissue responses. Integrating *in vivo* conditions into computational models could further enhance the relevance of the results to clinical settings.

4. Conclusions

This study provides a detailed examination of the relationship between aging and changes in the anterior segment morphology, particularly focusing on the CCT, PCT, ACA, IT, and CBA. By integrating advanced imaging techniques such as LSFM and CFD, we have captured

significant age-related trends in these structures, offering new understandings of how aging may contribute to influencing IOP regulation and the biomechanics of the anterior segment. Our findings reveal that CCT and PCT exhibit a tendency to decrease with age, while the ACA shows a potential decline that could possibly impact aqueous humor dynamics. The correlation between CCT and PCT indicates a more complex biomechanical relationship, suggesting that changes in central corneal structure can influence peripheral corneal regions. Contrary to expectations, the CBA displayed remarkable stability with age, indicating that the ciliary body's function in aqueous humor production may be less affected by aging compared to other anterior segment structures. This observation suggests that age-related changes in IOP regulation might be driven more by alterations in the cornea and anterior chamber than by the ciliary body itself. The fluid dynamics analysis demonstrated that both velocity and wall shear stress decrease with age. While the study offers valuable information, the small sample size and lack of consideration for sex differences underscore the need for cautious interpretation. Future research should involve a larger, more diverse cohort, accounting for gender and other biological variables, to provide a more comprehensive understanding of how aging affects anterior segment morphology and aqueous humor dynamics. These findings have significant implications for diagnosing and managing age-related ocular conditions such as glaucoma, underscoring the importance of age-specific considerations in clinical assessments and treatment strategies.

CRediT authorship contribution statement

Alireza Karimi: Writing – review & editing, Writing – original draft, Visualization, Validation, Supervision, Software, Resources, Project administration, Methodology, Investigation, Funding acquisition, Formal analysis, Data curation, Conceptualization. **Marie Darche:** Data curation, Conceptualization. **Ansel Stanik:** Software. **Reza Razaghi:** Methodology, Software. **Iman Mirafzal:** Software. **Kamran Hassani:** Software. **Mojtaba Hassani:** Software. **Elizabeth White:** Methodology. **Ivana Gantar:** Visualization. **Stéphane Pagès:** Visualization. **Laura Batti:** Visualization. **Ted S. Acott:** . **Michel Paques:** Investigation.

Declaration of Competing Interest

The authors declare that they have no known competing financial interests or personal relationships that could have appeared to influence the work reported in this paper.

Acknowledgments

This work was supported by funding from NIH/NEI R01EY036011, NIH/NEI P30EY010572, Lewis Rudin Glaucoma Prize and Research to Prevent Blindness Foundation (New York, New York) grant to the Casey Eye Institute. Funded by the Institut Hospitalo-Universitaire FORe-SIGHT (ANR-18-IAHU-01), Region Ile-de-France (EX047007 - SESAME 2019) and Association Contre l'OVR. The funding organizations had no role in the design or conduct of this research.

References

[1] Weinreb RN, Aung T, Medeiros FA. The pathophysiology and treatment of glaucoma: a review. JAMA 2014;311:1901–11.
[2] Quigley HA, Vitale S. Models of open-angle glaucoma prevalence and incidence in the United States. Invest Ophthalmol Vis Sci 1997;38:83–91.
[3] Group EDPR. Prevalence of open-angle glaucoma among adults in the United States. Arch Ophthalmol 2004;122:532.
[4] Sherratt MJ. Tissue elasticity and the ageing elastic fibre. Age (Dordr) 2009;31:305–25.
[5] Natali AN, Pavan PG, Carniel EL, Dario P, Izzo I. Characterization of soft tissue mechanics with aging. IEEE Eng Med Biol Mag 2008;27:15–22.
[6] Humphrey JD. Continuum biomechanics of soft biological tissues. Proceedings of the Royal Society of London Series A: Mathematical, Physical and Engineering Sciences. 2003;459:3-46.
[7] Holzapfel GA. Biomechanics of soft tissue. The handbook of materials behavior models 2001;3:1049–63.
[8] Buckwalter JA, Woo SL, Goldberg VM, Hadley EC, Booth F, Oegema TR, et al. Soft-tissue aging and musculoskeletal function. J Bone Joint Surg 1993;75:1533–48.
[9] Lütjen-Drecoll E, Dietl T, Futa R, Rohen J. Age changes of the trabecular meshwork. A preliminary morphometric study. The Structure of the Eye 1982:341–8.
[10] Armaly MF. The genetic determination of ocular pressure in the normal eye. Arch Ophthalmol 1967;78:187–92.
[11] Becker B. The decline in aqueous secretion and outflow facility with age. Am J Ophthalmol 1958;46:731–6.
[12] Brubaker RF, Nagataki S, Townsend DJ, Burns RR, Higgins RG, Wentworth W. The effect of age on aqueous humor formation in man. Ophthalmology 1981;88:283–8.
[13] Gaasterland D, Kupfer C, Ross K, Gabelnick HL. Studies of aqueous humor dynamics in man: III. Measurements in young normal subjects using norepinephrine and isoproterenol. Invest Ophthalmol Vis Sci 1973;12:267–79.
[14] Toris CB, Yablonski ME, Wang YL, Camras CB. Aqueous humor dynamics in the aging human eye. Am J Ophthalmol 1999;127:407–12.
[15] Nomura H, Ando F, Niino N, Shimokata H, Miyake Y. The relationship between age and intraocular pressure in a Japanese population: the influence of central corneal thickness. Curr Eye Res 2002;24:81–5.
[16] Shiose Y. Intraocular pressure: new perspectives. Surv Ophthalmol 1990;34:413–35.
[17] Hiller R, Sperduto RD, Krueger DE. Race, iris pigmentation, and intraocular pressure. Am J Epidemiol 1982;115:674–83.
[18] Klein BE, Klein R, Linton KL. Intraocular pressure in an American community. The Beaver Dam Eye Study. Invest Ophthalmol Vis Sci 1992;33:2224–8.
[19] Gaasterland D, Kupfer C, Milton R, Ross K, McCain L, MacLellan H. Studies of aqueous humour dynamics in man VI. Effect of age upon parameters of intraocular pressure in normal human eyes. Exp Eye Res 1978;26:651–6.
[20] Kupfer C. Clinical significance of pseudofacility. Sanford R. Gifford Memorial Lecture. Am J Ophthalmol 1973;75:193–204.
[21] Croft MA, Oyen MJ, Gange SJ, Fisher MR, Kaufman PL. Aging effects on accommodation and outflow facility responses to pilocarpine in humans. Arch Ophthalmol 1996;114:586–92.
[22] Townsend D, Brubaker RF. Immediate effect of epinephrine on aqueous formation in the normal human eye as measured by fluorophotometry. Invest Ophthalmol Vis Sci 1980;19:256–66.
[23] Bloom JN, Levene RZ, Thomas G, Kimura R. Fluorophotometry and the rate of aqueous flow in man. I. Instrumentation and normal values. Arch Ophthalmol 1976;94:435–43.
[24] Diestelhorst M, Kriegistein G. Does aqueous humor secretion decrease with age? Int Ophthalmol 1992;16:305–9.
[25] Armaly MF. The consistency of the 1955 calibration for various tonometer weights. Am J Ophthalmol 1959;48:602–11.
[26] Bito LZ, DeRousseau CJ, Kaufman PL, Bito JW. Age-dependent loss of accommodative amplitude in rhesus monkeys: an animal model for presbyopia. Invest Ophthalmol Vis Sci 1982;23:23–31.
[27] Kotecha A, Elsheikh A, Roberts CR, Zhu H, Garway-Heath DF. Corneal thickness- and age-related biomechanical properties of the cornea measured with the ocular response analyzer. Invest Ophthalmol Vis Sci 2006;47:5337–47.
[28] Galgauskas S, Norvydaite D, Krasauskaite D, Stech S, Asoklis RS. Age-related changes in corneal thickness and endothelial characteristics. Clin Interv Aging 2013;8:1445–50.
[29] Pan C, Cai R, Quacquarelli FP, Ghasemigharagoz A, Lourbopoulos A, Matryba P, et al. Shrinkage-mediated imaging of entire organs and organisms using uDISCO. Nat Methods 2016;13:859–67.
[30] Renier N, Wu Z, Simon DJ, Yang J, Ariel P, Tessier-Lavigne M. iDISCO: a simple, rapid method to immunolabel large tissue samples for volume imaging. Cell 2014;159:896–910.
[31] Tomer R, Khairy K, Amat F, Keller PJ. Quantitative high-speed imaging of entire developing embryos with simultaneous multiview light-sheet microscopy. Nat Methods 2012;9:755–63.
[32] Silvestri L, Costantini I, Sacconi L, Pavone FS. Clearing of fixed tissue: a review from a microscopist's perspective. J Biomed Opt 2016;21:081205.
[33] Belle M, Godefroy D, Dominici C, Heitz-Marchaland C, Zelina P, Hellal F, et al. A simple method for 3D analysis of immunolabeled axonal tracts in a transparent nervous system. Cell Report 2014;9:1191–201.
[34] de Bakker BS, de Jong KH, Hagoort J, de Bree K, Besselink CT, de Kanter FE, et al. An interactive three-dimensional digital atlas and quantitative database of human development. Science 2016;354.
[35] Weiss KR, Voigt FF, Shepherd DP, Huisken J. Tutorial: practical considerations for tissue clearing and imaging. Nat Protoc 2021;16:2732–48.
[36] Mai H, Rong Z, Zhao S, Cai R, Steinke H, Bechmann I, et al. Scalable tissue labeling and clearing of intact human organs. Nat Protoc 2022;17:2188–215.
[37] Boutin ME, Hampton C, Quinn R, Ferrer M, Song MJ. 3D Engineering of Ocular Tissues for Disease Modeling and Drug Testing. Adv Exp Med Biol 2019;1186:171–93.
[38] Susaki EA, Ueda HR. Whole-body and Whole-Organ Clearing and Imaging Techniques with Single-Cell Resolution: Toward Organism-Level Systems Biology in Mammals. Cell Chem Biol 2016;23:137–57.
[39] Graw J. Eye development. Curr Top Dev Biol 2010;90:343–86.
[40] Gurdita A, Nickerson PEB, Pokrajac NT, Ortin-Martinez A, Samuel Tsai EL, Comanita L, et al. InVision: An optimized tissue clearing approach for three-dimensional imaging and analysis of intact rodent eyes. iScience 2021;24:102905.

[41] Henning Y, Osadnik C, Malkemper EP. EyeCi: Optical clearing and imaging of immunolabeled mouse eyes using light-sheet fluorescence microscopy. Exp Eye Res 2019;180:137–45.
[42] Ye Y, Dinh Duong TA, Saito K, Shinmyo Y, Ichikawa Y, Higashide T, et al. Visualization of the Retina in Intact Eyes of Mice and Ferrets Using a Tissue Clearing Method. Transl Vis Sci Technol 2020;9:1.
[43] Lu W, Pei Z, Hu W, Tan C, Tong X, Feng Y, et al. Recent progress in optical clearing of eye tissues. Exp Eye Res 2021;212:108796.
[44] Vigouroux RJ, Cesar Q, Chedotal A, Nguyen-Ba-Charvet KT. Revisiting the role of Dcc in visual system development with a novel eye clearing method. Elife 2020;9.
[45] Darche M, Verschueren A, Belle M, Boucherit L, Fouquet S, Sahel JA, et al. Three-dimensional characterization of developing and adult ocular vasculature in mice using in toto clearing. Commun Biol 2022;5:1135.
[46] Waxman S, Loewen RT, Dang Y, Watkins SC, Watson AM, Loewen NA. High-Resolution, Three-Dimensional Reconstruction of the Outflow Tract Demonstrates Segmental Differences in Cleared Eyes. Invest Ophthalmol Vis Sci 2018;59:2371–80.
[47] Hohberger B, Baumgart C, Bergua A. Optical clearing of the eye using the See Deep Brain technique. Eye (Lond) 2017;31:1496–502.
[48] Wang K, Read AT, Sulchek T, Ethier CR. Trabecular meshwork stiffness in glaucoma. Exp Eye Res 2017;158:3–12.
[49] Karimi A, Razaghi R, Rahmati SM, Downs JC, Acott TS, Wang RK, et al. Modeling the biomechanics of the conventional aqueous outflow pathway microstructure in the human eye. Comput Methods Programs Biomed 2022;221:106922.
[50] Karimi A, Razaghi R, D'Costa SD, Torbati S, Ebrahimi S, Rahmati SM, et al. Implementing new computational methods for the study of JCT and SC inner wall basement membrane biomechanics and hydrodynamics. Comput Methods Programs Biomed 2024;243:107909.
[51] Karimi A, Crouch DJ, Razaghi R, Crawford Downs J, Acott TS, Kelley MJ, et al. Morphological and biomechanical analyses of the human healthy and glaucomatous aqueous outflow pathway: Imaging-to-modeling. Comput Methods Programs Biomed 2023;236:107485.
[52] Karimi A, Halabian M, Razaghi R, Downs JC, Kelley MJ, Acott TS. Modeling the Endothelial Glycocalyx Layer in the Human Conventional Aqueous Outflow Pathway. Cells 2022;11:3925.
[53] Karimi A, Rahmati SM, Razaghi R, Crawford Downs J, Acott TS, Wang RK, et al. Biomechanics of human trabecular meshwork in healthy and glaucoma eyes via dynamic Schlemm's canal pressurization. Comput Methods Programs Biomed 2022;221:106921.
[54] Karimi A, Razaghi R, Kelley MJ, Acott TS, Gong H. Biomechanics of the jct and sc inner wall endothelial cells with their basement membrane using 3d serial block-face scanning electron microscopy. Bioengineering 2023;10:1038.
[55] Karimi A, Razaghi R, Stanik A, Daniel D'costa S, Mirafzal I, Kelley MJ, et al. High-resolution modeling of aqueous humor dynamics in the conventional outflow pathway of a normal human donor eye. Comput Methods Programs Biomed 2024;260:108538.
[56] Darche M, Borella Y, Verschueren A, Gantar I, Pages S, Batti L, et al. Light sheet fluorescence microscopy of cleared human eyes. Commun Biol 2023;6:1025.
[57] Murray E, Cho JH, Goodwin D, Ku T, Swaney J, Kim SY, et al. Simple, Scalable Proteomic Imaging for High-Dimensional Profiling of Intact Systems. Cell 2015;163:1500–14.
[58] Voigt FF, Kirschenbaum D, Platonova E, Pages S, Campbell RAA, Kastli R, et al. The mesoSPIM initiative: open-source light-sheet microscopes for imaging cleared tissue. Nat Methods 2019;16:1105–8.
[59] Karimi A, Rahmati SM, Grytz RG, Girkin CA, Downs JC. Modeling the biomechanics of the lamina cribrosa microstructure in the human eye. Acta Biomater 2021;134:357–78.
[60] Karimi A, Khan S, Razaghi R, Rahmati SM, Gathara M, Tudisco E, et al. Developing an experimental-computational workflow to study the biomechanics of the human conventional aqueous outflow pathway. Acta Biomater 2023.
[61] Karimi A, Khan S, Razaghi R, Aga M, Rahmati SM, White E, et al. Segmental biomechanics of the normal and glaucomatous human aqueous outflow pathway. Acta Biomater 2024;173:148–66.
[62] Dubbelman M, Van der Heijde GL. The shape of the aging human lens: curvature, equivalent refractive index and the lens paradox. Vision Res 2001;41:1867–77.
[63] Avtar R, Srivastava R. Modelling aqueous humor outflow through trabecular meshwork. Appl Math Comput 2007;189:734–45.
[64] Villamarin A, Roy S, Hasballa R, Vardoulis O, Reymond P, Stergiopulos N. 3D simulation of the aqueous flow in the human eye. Med Eng Phys 2012;34:1462–70.
[65] Xie X, Corradetti G, Song A, Pardeshi A, Sultan W, Lee JY, et al. Age- and refraction-related changes in anterior segment anatomical structures measured by swept-source anterior segment OCT. PLoS One 2020;15:e0240110.
[66] Nongpiur ME, Haaland BA, Friedman DS, Perera SA, He M, Foo LL, et al. Classification algorithms based on anterior segment optical coherence tomography measurements for detection of angle closure. Ophthalmology 2013;120:48–54.